Nanoscale

Multi-functional MnO_2 nanomaterials for photo-activated applications by a plasma-assisted fabrication route

Journal:	*Nanoscale*
Manuscript ID	Draft
Article Type:	Paper
Date Submitted by the Author:	n/a

Complete List of Authors:	Barreca, Davide; CNR-ICMATE and INSTM, Department of Chemical Sciences, padova University Gri, Filippo; Padova University and INSTM, Department of Chemical Sciences Gasparotto, Alberto; Padova University and INSTM, Department of Chemical Sciences Carraro, Giorgio; Padova University and INSTM, Department of Chemical Sciences Bigiani, Lorenzo; Padova University and INSTM, Department of Chemical Sciences Altantzis, Thomas; University of Antwerp, EMAT Zener, Bostjan; University of Ljubljana, Faculty of Chemistry and Chemical Technology Lavrencic Stangar, Urska; University of Ljubljana, Faculty of Chemistry and Chemical Technology Alessi, Bruno; Ulster University, Nanotechnology & Integrated Bio-Engineering Centre (NIBEC) Padmanaban, Dilli; Ulster University, Nanotechnology & Integrated Bio-Engineering Centre (NIBEC) Mariotti, Davide; Ulster University, Nanotechnology & Integrated Bio-Engineering Centre (NIBEC) Maccato, Chiara; Padova University and INSTM, Department of Chemical Sciences

National Research Council - CNR
Institute of Condensed Matter Chemistry and Technologies for Energy - ICMATE
Padova

August the 10th, 2018

Dear Editor,
we are pleased to submit you our manuscript entitled

Multi-functional MnO_2 nanomaterials for photo-activated applications by a plasma-assisted fabrication route

By Davide Barreca, Filippo Gri, Alberto Gasparotto, Giorgio Carraro, Lorenzo Bigiani, Thomas Altantzis, Boštjan Žener, Urška Lavrenčič Štangar, Bruno Alessi, Dilli Babu Padmanaban, Davide Mariotti, Chiara Maccato,

to be considered for publication in *Nanoscale* as a paper, if acceptable. On behalf of all co-authors, we confirm hereby that the present manuscript is original/unpublished and that we have not previously submitted or published it in any other journal or conference proceedings.

Over the last decade, photo-activated processes assisted by semiconducting materials have been widely recognized as environmentally friendly routes for purification/cleaning technologies, with particular regard to the degradation of wastewater pollutants and to the implementation of anti-fogging and self-cleaning end-uses. In this regard, an ongoing open challenge is the use of multi-functional platforms for both kinds of applications and based on supported metal oxide nanomaterials, that offer a broader perspective for property tailoring and an easier post-use recovery than powdered counterparts.

In this context, the present work reports on a single-step plasma enhanced-chemical vapor deposition route for the production of F-doped MnO_2 nanomaterials at temperatures between 100 and 400 °C. In a nut-shell, the proposed approach yields β-MnO_2 nanosystems with morphology and chemical composition finely tunable as a function of growth temperature, directly affecting the optical functional properties of the resulting materials. Preliminary photocatalytic tests highlight the possibility of finely tailoring nanomaterial performances, which resulted from a complex interplay between nano-organization, fluorine content and optical absorption properties. The system activity even under the sole Vis irradiation paves the way to the utilization of natural sunlight to activate the target processes, in the framework of an improved environmental sustainability.

The versatility in controlling the system behavior by modifying the synthesis conditions represent an interesting starting point for future implementations of the present materials. In perspective,

National Research Council - CNR
Institute of Condensed Matter Chemistry and Technologies for Energy - ICMATE
Padova

these results are of doubtless practical significance in the development of multi-functional photocatalysts for smart stimuli-responsive applications and wastewater purification.

For the above reasons, we expect that the present work can offer to a large community of scientists a valuable example about the importance of multi-functional nanomaterial design for photo-activated applications, meeting the high scientific standards and the cutting-edge results request of *Nanoscale.* We hope that the Editorial Board and the Reviewers will agree on the general interest of this study.

We look forward to the opportunity to respond to the Referee reports, and remain awaiting for your kind response in due course.

Thank you very much in advance for your kind attention,

Best regards,

Davide Barreca

Chiara Maccato

Davide Barreca, Ph. D.
Senior Research Scientist
ICMATE-CNR c/o Department of Chemical Sciences, Padova University
Via Marzolo 1, I-35131 Padova, ITALY
Phone: +39-049-8275170
E-mail: davide.barreca@unipd.it

Prof. Chiara Maccato
Department of Chemical Sciences, Padova University and INSTM
Via Marzolo 1, I-35131 Padova, ITALY
Phone: +39-049-8275234
E-mail: chiara.maccato@unipd.it
http://www.chimica.unipd.it/multi-functional-material-group/

Table of Contents

Multi-functional MnO_2 nanomaterials for photo-activated applications by a plasma-assisted fabrication route

Davide Barreca,*[a] Filippo Gri,[b] Alberto Gasparotto,[b] Giorgio Carraro,[b] Lorenzo Bigiani,[b] Thomas Altantzis,[c] Bostjan Zener,[d] Urška Lavrenčič Štangar,[d,e] Bruno Alessi,[f] Dilli Babu Padmanaban,[f] Davide Mariotti[f] and Chiara Maccato*[b]

[a] *CNR-ICMATE and INSTM, Department of Chemical Sciences, Padova University, Via Marzolo 1, 35131 Padova, Italy*
[b] *Department of Chemical Sciences, Padova University and INSTM, Via Marzolo 1, 35131 Padova, Italy*
[c] *EMAT, University of Antwerp, 2020 Antwerp, Belgium*
[d] *Faculty of Chemistry and Chemical Technology, University of Ljubljana, 1000 Ljubljana, Slovenia*
[e] *Laboratory for Environmental and Life Sciences, University of Nova Gorica, 5000 Nova Gorica, Slovenia*
[f] *Nanotechnology & Integrated Bio-Engineering Centre (NIBEC), Ulster University, BT37 0QB, UK*
* Corresponding authors. E-mail: davide.barreca@unipd.it; chiara.maccato@unipd.it

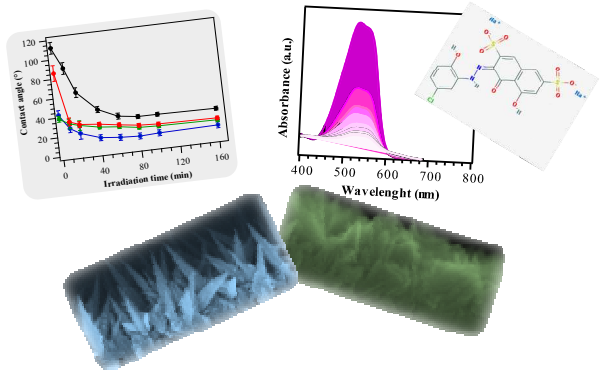

F-doped β-MnO_2 nanomaterials fabricated by a one-step plasma-assisted route display attractive functional performances in view of photo-activated self-cleaning/antifogging applications and wastewater treatment.

Nanoscale

PAPER

Multi-functional MnO_2 nanomaterials for photo-activated applications by a plasma-assisted fabrication route

Davide Barreca,*[a] Filippo Gri,[b] Alberto Gasparotto,[b] Giorgio Carraro,[b] Lorenzo Bigiani,[b] Thomas Altantzis,[c] Boštjan Žener,[d] Urška Lavrenčič Štangar,[d,e] Bruno Alessi,[f] Dilli Babu Padmanaban,[f] Davide Mariotti[f] and Chiara Maccato,*[b]

Received 00th January 20xx,
Accepted 00th January 20xx

DOI: 10.1039/x0xx00000x

www.rsc.org/

Supported MnO_2-based nanomaterials were fabricated on fluorine-doped tin oxide substrates by plasma enhanced-chemical vapor deposition (PE-CVD) between 100 °C and 400 °C, starting from a fluorinated Mn(II) diamine diketonate precursor. Growth experiments yielded β-MnO_2 nanosystems with hierarchical morphology tuneable from dendritic structures to quasi-1D nanosystems as a function of growth temperature, whose variation enabled also a concomitant tailoring of the system fluorine content, and of the optical absorption and band gap. Preliminary photocatalytic tests were aimed at the investigation of photoinduced hydrophilic (PH) and solid phase photocatalytic (PC) performances of the present nanomaterials, as well as at the photodegradation of Plasmocorinth B azo-dye aqueous solutions. The obtained findings highlighted an attractive system photoactivity even under visible light, finely taylored by fluorine content, morphological organization and optical properties of the prepared nanostructures. The results indicate that the synthesized MnO_2 nanosystems have potential applications as advanced smart material for anti-fogging/self-cleaning applications and water purification.

1. Introduction

Photoactivated processes have been widely recognized as cost-effective and environmentally friendly routes for both renewable energy generation and purification/cleaning technologies.[1-3] In particular, a great attention has been devoted to the degradation of persistent pollutants in effluent wastewaters, such as dyes from textile, paper and pharmaceutical industries, into harmless products.[4-6] In addition, increasing efforts have been focused on photoinduced anti-fogging and self-cleaning applications promoted by suitable functional systems, for which surface adsorption phenomena and hydrophobic/hydrophilic properties directly affect functional performances.[7, 8]

Among the possible candidate materials, (MnO_2) is an important transition metal oxide possessing various polymorphs, such as α-, β-, γ- and δ-MnO_2,[9-18] and has been the subject of several studies. In fact, thanks to the appealing variety of chemical and physical properties, MnO_2 materials keep their signature in many fields, such as Li-ion batteries, electrode materials for supercapacitors, gas sensors, adsorbent and heterogeneous catalysts.[5, 9, 10, 19-28] In addition, their band gap (E_G ≈ 1.5-2.7 eV, depending on the crystal phase and preparation process)[1, 2, 20, 29] enables to utilize the renewable and largely available solar energy for photocatalytic applications,[5, 13] differently from titania-based materials, whose absorption is limited to the UV spectral range.[13, 30] In fact, Mn(IV) and Ti(IV) oxides possess many similarities, including the presence of O defects and the basic structural unit, MO_6 (with M = Mn or Ti), being the *leitmotiv* of their various polymorphs [31]. Therefore, MnO_2-based systems could be usefully exploited in curbing environmental pollution and promoting water purification and safety, thanks also to their low toxicity, moderate price and high activity.[6, 15, 32-34] So far, MnO_2 materials have been used for the photodegradation of various organic dyes in wastewater.[1, 5, 6, 11, 13, 34] In a different way, reports on the reversible hydrophobic/hydrophilic switching and on solid phase photoactivated pollutant degradation have been devoted mainly to TiO_2[4, 35, 36] and other oxide materials,[7, 8] but, to the best of our knowledge, no MnO_2-based systems have ever been investigated for such applications.

As a general rule, the obtainment of pure crystallographic phases is highly desirable to control MnO_2 functional properties, though being an open challenge due to the system structural and morphological complexity.[14, 19, 21, 30, 37] In addition, MnO_2 properties are directly influenced by their nano-organization (nanorods, nanoflowers, nanotubes, nanosheets,...[9, 11, 13, 22, 38]), which, in turn, can be tailored by the adopted synthetic method.[12, 16, 33] As a consequence, efforts have been dedicated to the fabrication of low-dimensional MnO_2 systems by various techniques,[29, 34, 39, 40] among which liquid-phase routes are by far the most used.[6, 9, 11, 14, 16, 32] However, several studies have been dedicated to powders,[5, 9, 10, 12, 26, 30, 40] whereas supported MnO_2 systems, though being undoubtedly preferable for various applications,[7, 36, 41, 42] are indeed much less investigated.[2, 20, 21, 43] In particular, although previous studies have been done on nanostructured β-MnO_2 as electrode, catalytic and magnetic materials,[16, 17, 22, 37-39, 43, 44] the functional investigation of this polymorph, especially in supported forms and for photoactivated applications, deserves further efforts.[6]

[a] CNR-ICMATE and INSTM, Department of Chemical Sciences, Padova University, Via Marzolo 1, 35131 Padova, Italy. E-mail: davide.barreca@unipd.it
[b] Department of Chemical Sciences, Padova University and INSTM, Via Marzolo 1, 35131 Padova, Italy. E-mail: chiara.maccato@unipd.it
[c] EMAT, University of Antwerp, 2020 Antwerp, Belgium
[d] Faculty of Chemistry and Chemical Technology, University of Ljubljana, 1000 Ljubljana, Slovenia
[e] Laboratory for Environmental and Life Sciences, University of Nova Gorica, 5000 Nova Gorica, Slovenia
[f] Nanotechnology & Integrated Bio-Engineering Centre (NIBEC), Ulster University, BT37 0QB, UK

† Electronic Supplementary Information (ESI) available: XPS, EDXS and AFM experimental data; KP results; details on photocatalytic tests. See DOI: 10.1039/x0xx00000x

Herein, we report on the preparation of phase-pure supported β-MnO_2 nanomaterials, whose applications in Vis-light photoactivated processes are scarce, by means of plasma-enhanced chemical vapor deposition (PE-CVD), exploiting the unique gas-phase and surface chemistry of cold plasmas.[8, 45] So far, only one work is available on the PE-CVD of MnO_x thin films, but the control of the phase composition has been proven to be difficult.[41] In particular, our attention is devoted to the fabrication of F-doped MnO_2 nanomaterials starting from a fluorinated Mn(II) precursor. As a matter of fact, fluorine doping has been demonstrated to favorably affect the structural, optical, electrical and catalytic properties of different oxides for various applications, such as gas sensing, Li-ion batteries and photocatalysis,[46-51] but it has never been reported so far for MnO_2-based materials. To this aim, one of the main novel character of this work is the synthesis of nanostructured β-MnO_2 with a fine control of F content and morphology as a function of the growth temperature. For the first time, the functional behavior of the developed systems is investigated in relation to: a) their photoinduced hydrophilicity (PH) and solid phase photocatalytic (PC) activity in methylstearate degradation,[7] in view of antifogging and self-cleaning applications; b) the photodegradation of aqueous solutions of the monoazo dye Plasmocorinth B, chosen as a model compound thanks to its environmental stability and the absence of colored degradation by-products, enabling to follow its decomposition by means of ultraviolet-visible (UV-Vis) spectroscopy.[36] The most attractive results in view of possible future implementations are presented and critically discussed as a function of material properties.

2. Experimental section

2.1 Synthesis

PE-CVD growth processes were performed using a two-electrode custom-built apparatus equipped with a radio frequency (RF) generator (ν = 13.56 MHz), adopting $Mn(tfa)_2$•TMEDA (tfa = 1,1,1-trifluoro-2,4-pentanedionate; TMEDA = *N*,*N*,*N*′,*N*′-tetramethylethylenediamine) as precursor.[52] Fluorine-doped tin oxide (FTO)-coated glass substrates (Aldrich®; ≈ 7 Ω/sq; FTO thickness ≈ 600 nm), subjected to an established pre-cleaning procedure,[53] were mounted on the grounded electrode, whereas RF-power was delivered to the second electrode. Electronic grade Ar and O_2 were used as plasma sources. The precursor was placed in an external glass vessel heated at 85°C by an oil bath and transported toward the deposition zone by an Ar flow (rate = 60 standard cubic centimeters per minute (sccm)) through feeding lines maintained at 150 °C. Two additional independent gas-lines were used to introduce Ar (rate = 15 sccm) and O_2 (rate = 5 sccm) directly into the reactor. For all depositions, the interelectrode distance, total pressure, RF-power and process duration were set at 6 cm, 1.0 mbar, 20 W and 60 min, respectively. The growth temperature was varied between 100 °C and 400 °C.

2.2 Characterization

X-ray diffraction (XRD) patterns were collected at an incidence angle of 1.0° on a Bruker D8 Advance X-ray diffractometer, equipped with a Göbel mirror and a Cu Kα X-ray source (40 kV, 40 mA).

X-ray photoelectron spectroscopy (XPS) analysis was performed using a Perkin–Elmer Φ 5600ci spectrometer and a standard Al Kα source (1486.6 eV). All binding energies (BEs; standard deviation = ± 0.2 eV) were referenced to the adventitious C1s component at 284.8 eV (Fig. S1†). After a Shirley-type background subtraction, atomic compositions were evaluated using Φ V5.4A sensitivity factors. When necessary, peak fitting was carried out by a least-squares procedure, using Gaussian–Lorentzian peak shapes. Ar^+ sputtering was carried out at 4.0 kV (Ar partial pressure = 5×10^{-8} mbar).

Field emission-scanning electron microscopy (FE-SEM) and energy dispersive X-ray spectroscopy (EDXS) measurements were carried out by a Zeiss SUPRA 40VP microscope, equipped with an Oxford INCA x-sight X-ray detector, at acceleration voltages between 10 kV and 20 kV. The ImageJ® software (http://imagej.nih.gov/ij/) was used to estimate deposit thickness and aggregate size.

Atomic force microscopy (AFM) images were obtained using a NT–MDT SPM Solver P47H–PRO instrument operating in tapping mode and in air. Root mean square (RMS) roughness values were calculated at a window size of 5 μm×5 μm, after background subtraction and plane fitting.

Cross-sectional samples for transmission electron microscopy (TEM) observations were prepared by focused ion beam (FIB-SEM, FEI HELIOS Nanolab 650). During sample preparation, due to the high length of the rods and their low packing density, a carbon coating and a Pt protective layer (high contrast regions between the rods) were deposited to embed the structures and prevent them from collapsing. Low and high magnification high angle annular dark field-scanning TEM (HAADF-STEM) images, selected area electron diffraction (SAED) patterns and EDXS elemental maps were acquired using an aberration corrected cubed FEI Titan electron microscope operated at 300 kV, equipped with the ChemiSTEM system.[54] Image acquisition was performed using probe convergence and detector collection inner semi-angles of 21 mrad and 55 mrad, respectively.

Optical spectra were recorded in transmittance mode using a Varian Cary 50 spectrophotometer, using bare FTO-coated glass substrate as a reference. In all cases, the substrate contribution was subtracted. The band gap (E_G) of the samples was evaluated using the equation:[3, 46, 47]

$$(\alpha h\nu)^n = A(h\nu - E_G) \quad (1)$$

where α and hν are the absorption coefficient and the photon energy, *A* is a constant and *n* = 2 (direct allowed transitions) for various MnO_2 polymorphs.[1, 20, 29, 34, 55] E_G values were obtained by extrapolating the straight portion of experimental curves to intersect the energy axis at α = 0.

Valence band XPS measurements were carried out in a Kratos Axis Ultra DLD X-ray photoelectron spectrometer at ≈ 10^{-9} mbar base pressure using an Al Kα (1486.6 eV) X-ray source operated at 15 kV and 10 mA, with an analyzer pass energy of 20 eV. For each sample, three measurement spots were taken with a spot size of 400 μm^2.

The absolute Fermi energy was determined by Kelvin probe (KP) measurements in atmosphere (KP Technologies APS04) with a 2 mm gold plated tip. A sputtered Au-on-Si reference was used for calibration of the tip work function and samples were kept in the dark for 24 h before analysis. Values of Fermi energy were scanned over a 16 mm^2 area and averaged to the final value.

2.3 Photocatalytic tests

PH properties were analyzed by following the evolution of H_2O contact angle (WCA) *vs*. illumination time. After storage in the dark, samples were subjected to front side irradiation by three UV lamps (Actinic BL, Philips, 2×20 W and 1×40 W). For each irradiation time, a water droplet (volume = 4 μL) was deposited on the sample surface and the average WCA values were determined by three independent measurements using a Theta Lite (Biolin Scientific) instrument. For solid phase PC oxidation tests, samples were preliminarily irradiated with the above UV light source in order to start from a "clean"

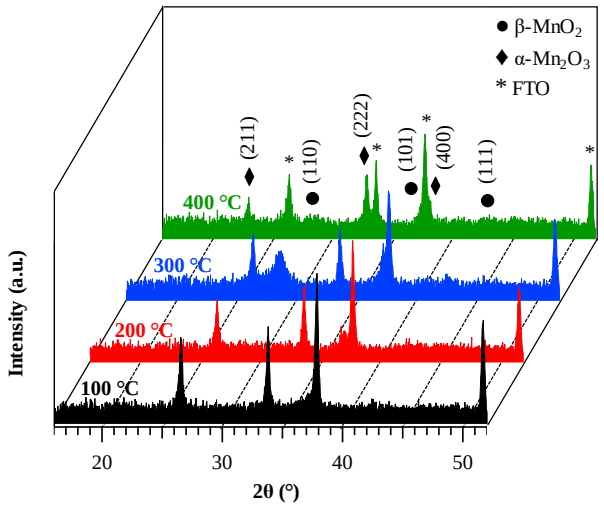

Fig. 1. XRD patterns of the target manganese oxide samples fabricated at different growth temperatures. Reflections pertaining to β-MnO_2, Mn_2O_3 and FTO substrate are marked for clarity.

hydrophilic surface, subsequently dip-coated with a 0.2 M solution of methyl stearate in *n*-hexane (withdrawal speed=10 cm×min^{-1}), and finally dried in air. This procedure resulted in the formation of a uniform fatty compound coating onto MnO_2 sample surface.[7] The photoinduced methyl stearate degradation was investigated by measuring WCA values *vs.* irradiation time, using the above reported conditions, immediately after application of the fatty compound layer. The reproducibility of the system activity was confirmed by three contamination/illumination cycles with WCA measurements.

Liquid phase photocatalytic tests were performed using a custom built photoreactor by immersing two identical samples (total geometrical area ≈5 cm × 5 cm) in 50 mL of a Plasmocorinth B dye solution (initial concentration = 2.3×10^{-5} M), continuously purged with gaseous oxygen throughout the process. Irradiation was carried out by a set of six different lamps arranged radially around the reactor [Blacklight Blue, Philips, for UV (36 W×m^{-2}) illumination; Lumilux De Luxe Daylight, Osram, for Vis (73 W×m^{-2}) illumination]. UV-Vis absorption spectra on the working solution were recorded by an Agilent Cary 60 UV-Vis spectrophotometer at regular time intervals (30 min), in order to investigate the dye photodegradation process. The photocatalytic activity was evaluated by monitoring the dye absorbance maximum (λ_{max} = 527 nm) as a function of irradiation time.[4, 42, 56] The residual dye content for each illumination time was calculated as:

$$A/A_0 \times 100 \ (= C/C_0 \times 100) \qquad (2)$$

with A (C) and A_0 (C_0) being the absorbance (concentration) values for the sample and the control solution, respectively.[34]

3. Results and discussion

3.1 Material characterization

The system structure was preliminarily analyzed by XRD (Fig. 1). The recorded patterns showed a limited number of broad and relatively weak diffraction peaks, as already observed for manganese oxide systems,[32] suggesting that the obtained specimens were formed by low-sized crystalline domains with highly defective structure,[13, 16] as also confirmed by TEM data (see below). For a growth temperature of 100°C, no appreciable signals were observed. In a different way, the sample grown at 200°C presented a weak reflection at 2θ ≈ 37.3° related to the (101) planes of β-MnO_2, the equilibrium phase of manganese dioxide at standard temperature and pressure[13, 44] (space group: tetragonal – $P4_2/mnm$, with lattice constants a = 4.39 and c = 2.87 Å).[33, 38, 40] The absence of the (110) peak at 2θ ≈ 28.7°, the most intense one in the reference powder spectrum for this polymorph,[57] suggested the possible occurrence of preferential orientation/texturing effects, although the modest diffracted intensity precluded more detailed observations. An increase of the growth temperature to 300 °C resulted in the appearance of the (110) β-MnO_2 reflection. Finally, at 400 °C the peaks located at 2θ = 23.2° and 33.0° were attributable respectively to (211) and (222) planes of body-centered cubic Mn_2O_3, whose presence accounted also for the low intensity (400) peak present as a shoulder on the FTO signal at 2θ ≈ 38.2°.[58] Nevertheless, a signature for β-MnO_2 presence is still provided by the reflection at 2θ ≈ 37.3°, manifesting as a shoulder on the more intense FTO signal. The co-presence of MnO_2 and Mn_2O_3, already observed during the liquid-phase synthesis of MnO_2 materials,[19, 31, 37] could be attributed to a partial MnO_2 thermal decomposition under these preparation conditions.[25, 59]

The surface chemical composition of the target systems was analyzed by XPS, yielding qualitatively similar results irrespective of the adopted deposition temperature. Survey spectra (Fig. 2a) displayed the presence of C (see also Fig. S1†), O, Mn and F signals. For a growth temperature ≤ 300°C, the Mn2p peak shape and position (Fig. 2b; BE($Mn2p_{3/2}$) = 642.7 eV; spin-orbit splitting = 11.5

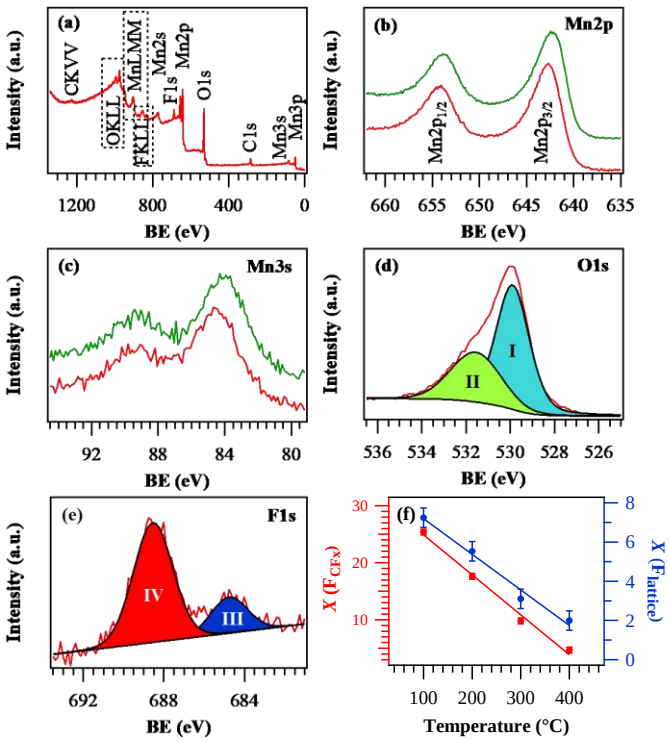

Fig. 2. (a) Surface wide-scan XPS survey of a representative MnO_2 sample synthesized at 200°C. The detailed Mn2p (b), Mn3s (c), O1s (d) and F1s (e) regions are also displayed. In (b) and (c), signals related to samples grown at 200 °C and 400 °C (red and green traces, respectively) are overlayed. (f) Evolution of fluorine pertaining to CF_x (red points, left axis) and lattice contributions (blue points, right axis) as a function of the adopted growth temperature. $X(F_{CFx})$ and $X(F_{lattice})$ were calculated as $X(F_{CFx})$ = {(% at. F_{CFx}) / [(% at. F_{CFx}) + (% at. Mn)]} × 100 and $X(F_{lattice})$ = {(% at. $F_{lattice}$) / [(% at. $F_{lattice}$) + (% at. Mn)]} × 100.

eV) were in agreement with the presence of MnO_2[12, 17, 21, 27, 31, 32] free from other manganese oxides in appreciable amounts, as also confirmed by the Mn3s multiplet splitting separation (Fig. 2c; 4.7 eV).[2, 15, 18, 33, 52] In a different way, at 400 °C the Mn2p spectrum (BE($Mn2p_{3/2}$) = 642.3 eV) along with the Mn3s band spacing (5.4 eV), was in line with the presence of Mn_2O_3.[24, 31, 40, 41] Nevertheless, the energy difference between BE($Mn2p_{3/2}$) maximum and the O1s lowest BE component (112.2 eV) was intermediate between those of Mn_2O_3 and MnO_2.[10, 17, 21, 25, 33]

The surface O/Mn atomic ratio (≈1.7-1.5 upon going from 100 °C to 400 °C) was lower than the stoichiometric value for manganese dioxide. The O1s peak (Fig. 2d) was decomposed by means of two components located at BE = 529.9 eV (I) and 531.6 eV (II). Whereas the former could be assigned to lattice oxygen in the Mn-O-Mn network,[6, 10, 15, 24, 43] the latter (typically ≈30% of the total O content) was due to the concurrence of hydroxyl groups and atmospheric oxygen adsorbed on surface defect sites.[9, 16, 30, 33, 59] Non-stoichiometric O vacancy-rich β-MnO_2 is indeed well documented[23, 37, 60] and the presence of "active oxygen" as lattice defects or adsorbed species on the surface has been reported to enhance its catalytic activity in various processes.[15, 24, 33, 37, 38] This feature favorably impacts even on the system photocatalytic performances, as discussed in detail in section 3.2. Finally, the surface F1s peak (Fig. 2e) was characterized by two components located at BE = 684.9 eV (III) and 688.5 eV (IV) The former, consistent with the presence of lattice F, revealed a successful fluorine incorporation into the oxide lattice as a result of the used fluorinated precursor in the plasma-assisted processes, leading to F-doped β-MnO_2 systems. The second component, related to precursor-derived CF_x groups (see also Fig. S1†),[49-53] could be removed after a few minutes of Ar^+ erosion, indicating that its presence was limited to the specimen surface. The uniform in-depth F distribution was confirmed by EDXS analyses (Fig. S2†). As can be observed from Fig. 2f, in line with previous works,[48, 50, 53] both F components underwent a decrease upon increasing the growth temperature, highlighting the possibility of tailoring F doping in the target MnO_2 systems by the sole variation of this parameter.

The nanosystem morphology, investigated by the combined use of FE-SEM and AFM surface analyses (Fig. 3), revealed a significant dependence on the adopted growth temperature. At 100 °C, the specimen was characterized by hierarchical dendritic structures (mean lateral dimension = 200 nm; overall deposit thickness = 330 nm) uniformly protruding from the FTO substrate, resulting from the assembly of low-sized lamellar aggregates (length and width = 75 nm and 20 nm, respectively). A similar morphology was obtained even for the sample grown at 200°C, although the formation of bigger and denser nanostructures (mean dimension = 230 nm; length and width of the lamellar aggregates = 115 nm and 30 nm, respectively) gave rise to a tightly packed cross-sectional arrangement. In a different way, a net morphological evolution took place for the specimen obtained at 300°C, that was characterized by pointed nanothorns (average length and diameter = 900 and 80 nm, respectively; mean aspect ratio = 11.2) protruding from a more compact underlayer

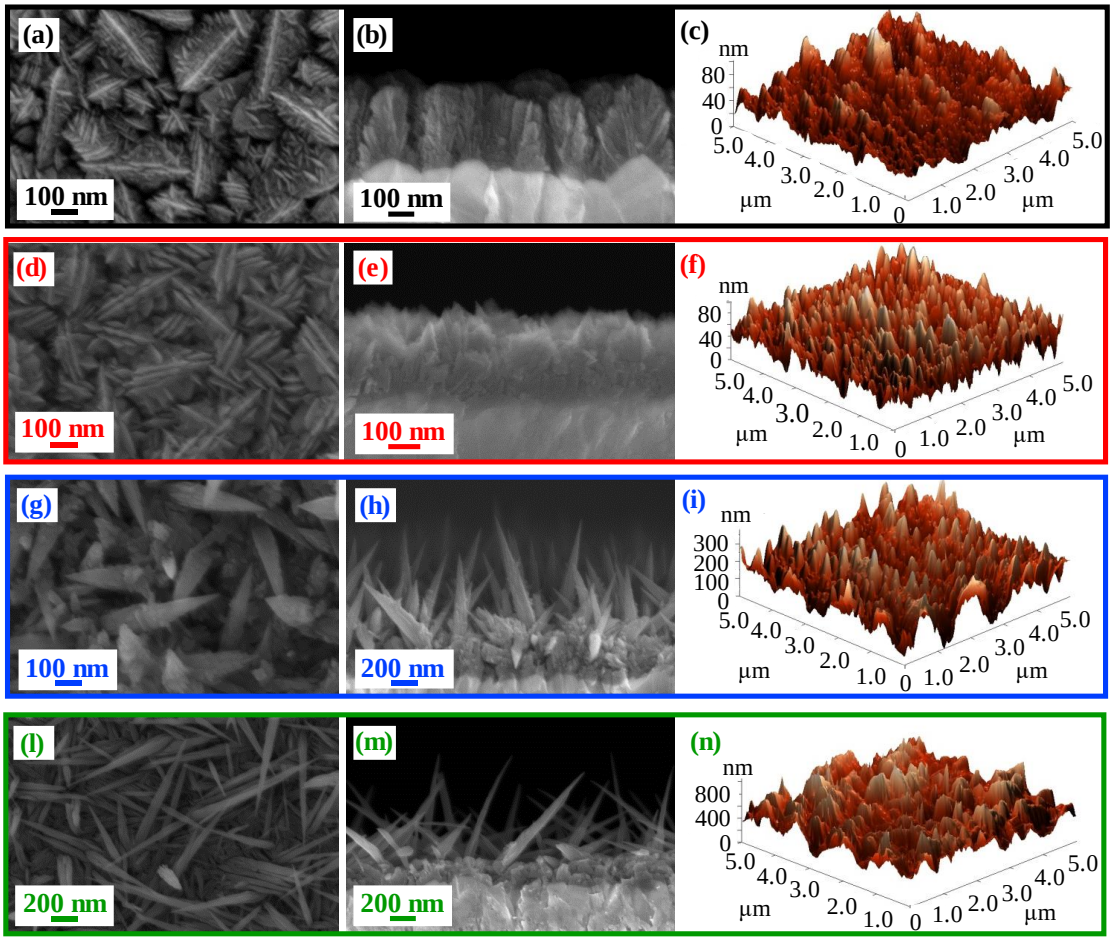

Fig. 3 (From left to right) Representative plane-view, cross-sectional FE-SEM images and AFM micrographs for β-MnO_2 nanomaterials obtained at different temperatures.

≈300 nm thick. At 400°C, the increased thermal energy supply produced more elongated quasi-1D nanostructures (average length and diameter = 900 nm and 50 nm, resulting in an aspect ratio of 18.0), with a thinner underlayer (≈180 nm). The morphology of the 300 °C and 400 °C deposits likely arises from the initial formation on the substrate of a granular layer, subsequently self-catalyzing the growth of anisotropic nanothorns in a process assisted by O deficiencies (see the above XPS data), resulting, in turn, from the material bombardment by O-related species.[45, 52] The surface topography was also probed by AFM, and images recorded on different sample areas enabled to ascertain surface homogeneity. The results, in line with FE-SEM data, confirmed the above discussed morphological evolution, highlighting the formation of highly rough materials. In particular, the calculated RMS roughness, that can be used as an estimation of surface area,[4, 7, 48] increased exponentially with the adopted growth temperature (Fig. S3†), *i.e.* with decreasing fluorine concentration,[47] leading to very high values at 400 °C. Thanks to their open and highly porous morphology, such nanostructures could be deemed to have potential advantages for photocatalytic applications, due to their reduced lateral size and high contact area with the reaction medium [1, 3, 34, 36].

In order to investigate in detail the system structure at the nanoscale, HAADF-STEM and EDXS analyses were carried out on representative specimens fabricated at 200 °C (Fig. 4) and 300 °C (Fig. 5). An overview HAADF-STEM cross-sectional image of the sample grown at 200 °C, together with EDXS elemental maps for Sn, Mn, O and F, is shown in Fig. 4a, revealing the FTO//MnO_2 stacking and a

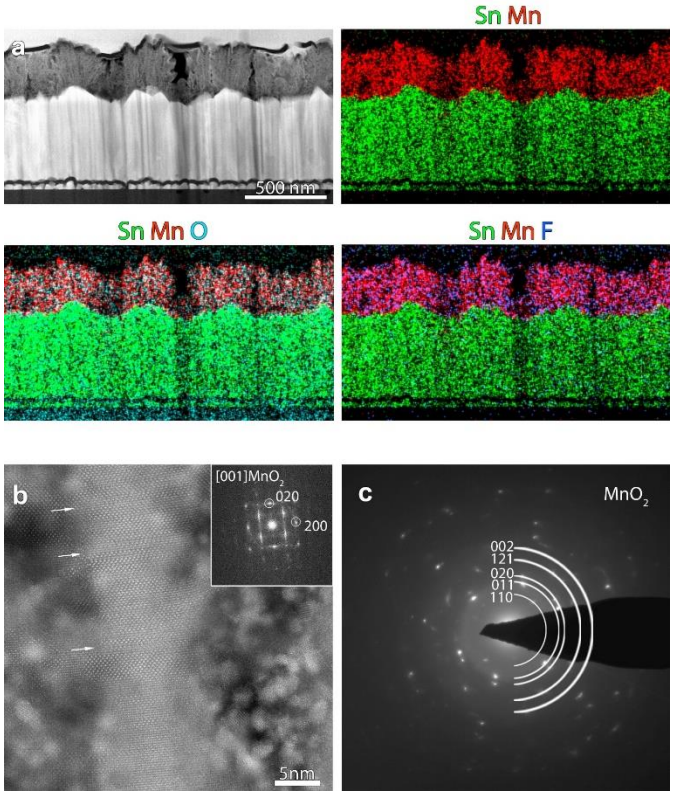

Fig. 4 (a) Cross-sectional HAADF-STEM image and corresponding EDXS elemental maps for a specimen fabricated at 200°C. (b) High resolution STEM image from the same sample together with the FFT pattern. The crystal is oriented along the [001] axis of the β-MnO_2 structure. The white arrows mark the presence of stacking faults. The high contrast particles in Fig. 4b are Pt nanoparticles from the protective layer deposited during FIB sample preparation. (c) SAED pattern from a region of the MnO_2 deposit in (a).

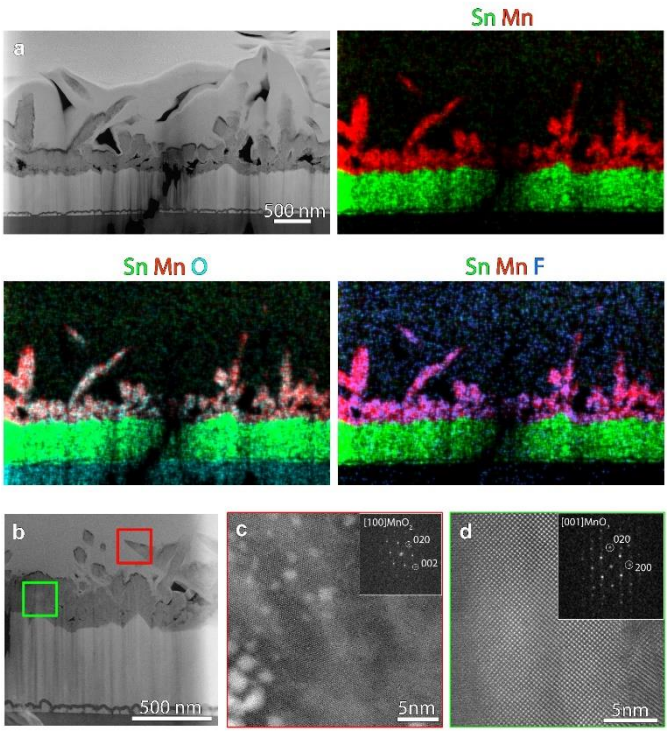

Fig. 5 (a) Cross-sectional HAADF-STEM image and corresponding EDXS elemental maps for a specimen fabricated at 300 °C. (b) Higher magnification HAADF-STEM image from a sample region. (c,d) High resolution STEM images from the thorns and the underlayer region, respectively, as indicated by the red and green squares marked in (b). FFT patterns (shown as insets) indicate that both structures correspond to β-MnO_2. The high contrast particles in Fig. 5c are Pt nanoparticles from the protective layer deposited during FIB sample preparation.

homogeneous spatial distribution of the analyzed elements. The presence of hierarchical dendritic structures is in line with the results obtained by FE-SEM (compare with Fig. 3). Fig. 4b displays a high resolution HAADF-STEM (*Z*-contrast) micrograph, together with the fast Fourier transform (FFT) pattern, shown as inset. The FFT corresponds to the [001] zone axis of the β-MnO_2 polymorph, the sole crystalline phase detected in the present specimen, in agreement with XRD results (see above). Many stacking faults could be observed, as indicated by the white arrows in Fig. 4b. SAED analysis (Fig. 4c) highlighted the polycrystalline nature of the target system, as can be noted by the presence of discontinuous circles.

Fig. 5a reports an overview HAADF-STEM image of the specimen grown at 300 °C, along with EDXS elemental maps. The micrographs evidence the assemblies of quasi-1D high aspect ratio nanothorns with pointed tips, growing from a relatively compact underlayer in contact with the FTO substrate, in accordance with FE-SEM observations. Fig. 5b reports a higher magnification HAADF-STEM image of a region of the sample, and Figs. 5c-d display representative high resolution HAADF-STEM images for the target nanothorns and the underlayer, collected in the regions marked in Fig. 5b by red and green squares, respectively. The corresponding FFT patterns (insets) reveal that both the nanothorn and underlayer structure correspond to the β-MnO_2 polymorph, in agreement with XRD and XPS analyses.

The fabricated materials were also analyzed by optical absorption spectroscopy (Fig. 6a). In general, the observed spectra displayed a prominent radiation absorption in the Vis range, of great importance for photocatalytic applications activated by Vis light (see

below). All the spectra were characterized by broadened absorption tail towards the near-infrared (NIR) region, consistent with the presence of O vacancies (see the above XPS data) and resulting in the formation of sub-band gap states.[46, 53] From Tauc plots (Fig. 6b), it was possible to extrapolate E_G values as 2.5 eV, 2.2 eV, 2.0 eV and 1.8 eV for growth temperatures of 100 °C, 200 °C, 300 °C and 400 °C. These values were blue-shifted with respect to literature data for MnO_2 (typically close to 1.8 eV,[1, 13, 60, 61]), a phenomenon that could be ascribed to the occurrence of size effects[29, 46] and to a modified carrier concentration when oxygen vacancies are saturated by fluorine. This explanation also accounts for the progressive increase of band gap values at the lowest deposition temperatures, resulting in a higher F content (see above and Fig. 2f).[47, 50, 53] For the specimen deposited at 400°C, the obtained band gap value (1.8 eV) was intermediate between those reported for MnO_2 and Mn_2O_3,[3, 13, 34] in line with the system composition (see above).

Fig. 6b also shows that the sample fabricated at 200°C possesses a higher absorption coefficient (α) with respect to the other ones, a phenomenon traced back to the best compromise between the system crystallinity and the higher lattice F content, whose introduction implies an enhancement of α values[49]. This result is of great importance, since a superior light absorption efficiency positively affects the functional behavior[36] (see below).

Fig. 6c displays a schematic band energy diagram reporting conduction band (CB), valence band (VB), and Fermi level (E_f) positions for the various samples. The energy band diagram of

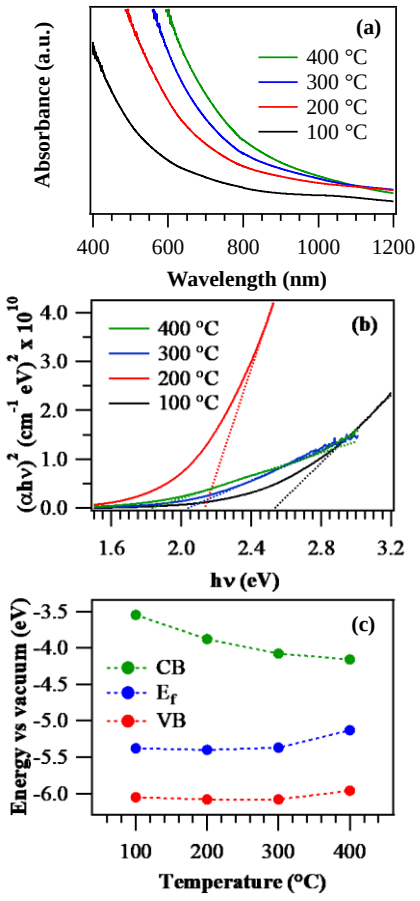

Fig. 6 Optical absorption spectra (a) and Tauc plots (b) for manganese oxide samples grown at different temperatures. (c) Schematic band energy diagram for the same specimens.

manganese oxides is very controversial in the literature, not only due to complications arising from the large number of possible polymorphs, but also because of the complex influence of oxygen-related defects, grain boundaries and, in the present case, also of fluorine doping [19, 37, 60, 62, 63]. In this work, the energy diagram in Fig. 6c was sketched basing on XPS, KP and optical absorption measurements (see above and Fig. S4†). Whereas the target samples show a rather high conductivity, the results reveal a band structure typical of a semiconductor. Similarly to our previous work on F-doped Fe_2O_3 [53], the present data suggest that the increase of band gap values with fluorine content was not due to a Moss Burnstein effect (involving the partial filling of CB and increase of *n*-type behavior with fluorine concentration), but to a different phenomenon, as testified by the progressive increase of the system *p*-type behavior at higher F loading (*i.e.* lower deposition temperature). In fact, oxygen vacancies yield occupied sub-band gap states above the VB edge, as suggested by optical absorption data (see above). Due to fluorine incorporation into the material and the subsequent formation of Mn-F bonds (as confirmed by XPS), these states become partially empty. Hence, they can accept electrons from MnO_2 valence band, generating holes in the latter. This phenomenon is likely to become predominant at higher F concentrations, explaining thus the enhanced *p*-type character for samples grown at lower temperatures.

3.2 Photoactivated properties

PH tests on the obtained systems were carried out by measuring the evolution of water contact angle as a function of irradiation time (Fig. 7a). As can be observed, all samples presented a relatively fast variation of their initial state upon UV exposure, yielding appreciably hydrophilic surfaces for sufficiently long irradiation. The typical time within which the final hydrophilic state is reached (< 1 h) is in line with previously reported data for other oxide-based materials obtained by CVD and PE-CVD routes [7, 8]. Nevertheless, the initial WCA value at the beginning of the process (in the absence of UV irradiation) results progressively lower for samples obtained at higher growth temperatures. This feature could be mainly traced back to the different fluorine content of the target specimens, which, as already discussed, decreases upon increasing the temperature (see Fig. 2f). In fact, the surface presence of a higher CF_x group content resulted in a more hydrophobic surface,[64] as observed for the samples obtained at 100 °C and 200°C (see also XPS data above). In addition, fluorine presence leads to a passivation of nanomaterial defects and, hence, to a reduced content of oxygen vacancies,[48, 50, 53] that are the key active sites for water chemisorption, with the

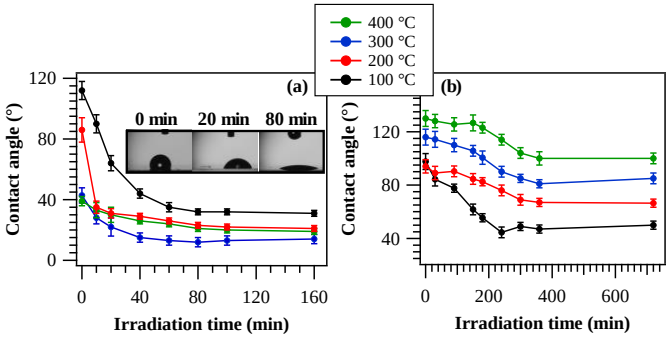

Fig. 7 (a) PH behavior of MnO_2 nanomaterials: WCA as a function of irradiation time. Inset: photographs of H_2O droplets on a specimen fabricated at 100 °C at different illumination stages. (b) PC behaviour for the same samples: water CA *vs*. irradiation time for methyl stearate-coated systems.

formation of new –OH groups.[4, 7, 8, 35] As a consequence, higherfluorine loadings result in an increased initial hydrophobicity. An additional concurrent contribution to the trend of the initial contact angles is provided by RMS roughness values, progressively increasing with the growth temperature (Fig. S3†).[7, 35]

As can be observed, the system behavior became more hydrophilic upon irradiation, with a direct dependence on the deposition temperature. The Δ(WCA) value (difference between the initial and final contact angles) is in fact reduced from ≈80 to ≈20° upon going from 100 °C to 400°C. The rationale for the above difference lies in the different fluorine content of the target materials, since an increase in F content (at 100 °C) results in an increase of the Lewis acidity of metal centers, beneficially affecting the system activity.[49] In addition, at the lowest temperatures, the higher F content is more effective in passivating material defects, reducing thus detrimental electron-hole recombination.[53] In a different way, carrier recombination processes are favored by lower band gap values, corresponding indeed to the less active samples fabricated at higher temperatures. Despite for the latter cases an RMS roughness would imply a higher active area (see above), it appears that this phenomenon (Fig. S3†) cannot efficiently counterbalance the above effects. In addition, the formation of Mn_2O_3/MnO_2 heterojunctions at 400 °C does not improve the separation of photogenerated charge carriers, due to the unfavorable band edge positions at the interface between these oxides (Fig. S5†). At the end of PH tests, samples were stored in the dark for 12 h and subsequent measurements of initial WCA values revealed the restore of initial surface characteristics, highlighting the reversibility of the discussed behavior.

In spite of the preliminary character of these studies, our results highlight that the target nanomaterials are active in photo-induced superhydrophilicity processes and that, in particular, the sample grown at 100 °C exhibited a superior activity with respect to a commercial Pilkington® Activ™ Glass, a reference standard for the target applications.[7] These results are of particular interest due to the MnO_2 environmentally friendly character and capability of harvesting solar radiation, differently from TiO_2 or ZnO, the most used platforms for such applications.

Solid phase PC performances of the target nanomaterials were examined in the photodecomposition of methyl stearate, a well-known model fatty compound, by monitoring WCA evolution *vs.* illumination time[7] (see the Experimental section; Fig. 7b). As a general rule, the starting WCA values were all higher than 90°, in accordance with the presence of the hydrophobic methyl stearate overlayer. In addition, the initial WCA values progressively increased with the adopted growth temperature, due to the concomitant increase of the system RMS roughness (see above), enhancing the system hydrophobicity.[7] In general, the material activity resulted directly dependent on the deposition temperature. In particular, the Δ(WCA) value decreased from ≈50° to ≈30° upon going from 100 °C to 400 °C, and even in the latter case the excursion was higher than that exhibited by the reference Pilkington® Activ™ Glass.[7] The best performances of the 100 °C-deposited sample could be mainly related to its higher lattice F content (see above and Fig. 2f), exerting a beneficial influence on the improvement of photocatalytic activity and conductivity and suppressing, in parallel, detrimental electron-hole recombination processes.[46, 49, 51, 53] In a different way, the other three samples were characterized by similar activities, traced back to a compromise between their different lattice F contents and RMS roughness values. Nevertheless, a predominant contribution of the latter was ruled out since, as already noted, the RMS roughness values showed an opposite trend with respect to that of Fig. 7b.

Finally, the liquid phase PC activity of the target specimens was tested in the degradation of Plasmocorinth B aqueous solutions as a function of illumination time. In all cases, control experiments revealed that no dye decomposition took place in the dark and/or in the absence of the target materials. Fig. 8a displays selected optical absorption spectra of a dye solution in the presence of a manganese dioxide specimen, showing a progressive absorbance decrease upon increasing UV irradiation time, and pointing out the effectiveness of these materials to quickly decompose the pollutant. The possible mechanism of the overall process is described in section S-1.5†. The

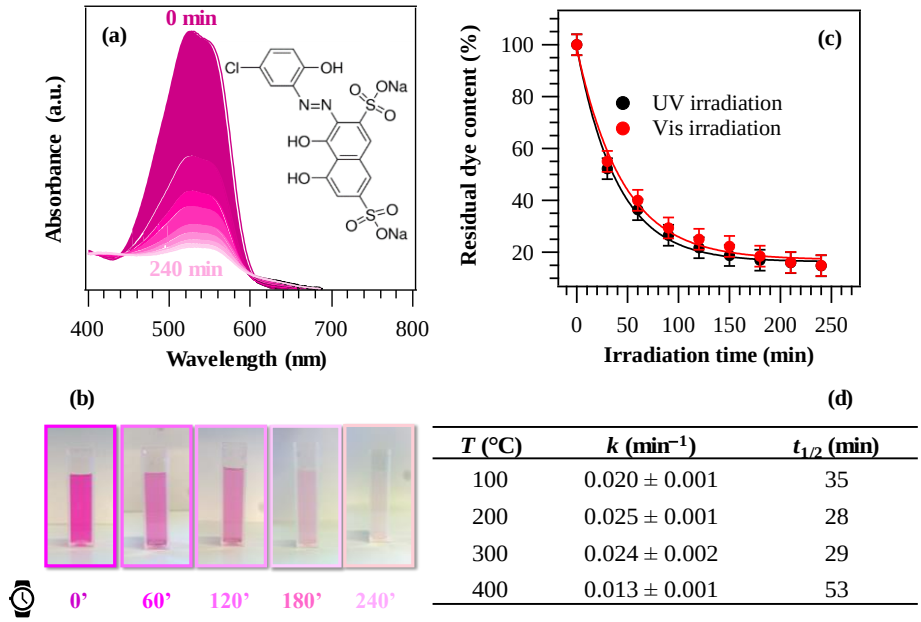

(d)

T (°C)	*k* (min^{-1})	$t_{1/2}$ (min)
100	0.020 ± 0.001	35
200	0.025 ± 0.001	28
300	0.024 ± 0.002	29
400	0.013 ± 0.001	53

Fig. 8 (a) Optical absorption spectra of Plasmocorinth B aqueous solutions (2.3×10^{-5} M) as a function of UV irradiation time in the presence of a β-MnO_2 specimen synthesized at 200 °C. (b) Solution photobleaching at different illumination times. (c) Photocatalytic performances in the degradation of Plasmocorinth B under UV and Vis illumination for a representative MnO_2 sample fabricated at 200 °C. (d) Values of the apparent kinetic constants and half-life times for specimens obtained at different temperatures.

solution fading due to dye degradation is visible also to the naked eye (Fig. 8b). Fig. 8c displays the relative Plasmocorinth B concentration *vs*. irradiation time in the presence of a representative MnO_2 sample. Photocatalytic dye decomposition was carried out utilizing not only UV, but even Vis light. The obtained results (Fig. 8c) revealed a comparable sample activity under both UV and Vis irradiation (see also kinetic constants and half-lives data in Table S1†), an interesting goal from an applicative point of view. In addition, cyclability tests (Fig. S6†) did not show any significant performance degradation, differently from previous studies [42], an issue of vital importance in view of practical applications.[4, 30, 32, 56]

As a general rule, all specimens were active in the target process and the dye decomposition followed a *pseudo*-first-order reaction kinetics, as usually reported in similar cases.[5, 6, 34] The values of apparent first-order rate constants and half-lives are reported in Fig. 8d. Such results were better than those exhibited in Plasmocorinth B photocatalytic oxidation over supported TiO_2 and M/TiO_2 (M = Ag, Au) films,[36, 42, 56] highlighting thus the potential of the present materials for use in photocatalytic dye degradation processes.

The obtained data suggest the following trend for the sample photocatalytic activity as a function of the material growth temperature: 400 °C < 100 °C < 300 °C ≈ 200 °C, different from that observed for data in Fig. 7. This result could be apparently surprising, since the specimen obtained at 400 °C was characterized by the highest roughness (*i.e.*, by a higher active area), and, at a first glance, it could have been expected to be the most active. However, the formation of MnO_2/Mn_2O_3 junctions, can promote the recombination of photogenerated electrons and holes, leading thus to a decreased photoactivity (Fig. S5†) The observed behavior suggested the concurrence of various factors in determining the system liquid phase photoactivity: *i)* the different radiation absorption; *ii)* the different lattice fluorine content; *iii)* the system optical band gaps, and *iv)* the RMS surface roughness values. In this regard, the specimen obtained at 200 °C turned out to be the most active, likely due to the best compromise between factors *i)-iv)*.

4. Conclusions

This work has reported on the PE-CVD fabrication of MnO_2 nanosystems from Ar-O_2 plasmas on FTO substrates. The use of a fluorinated Mn(II) molecular precursor enabled a homogeneous F doping of the target systems, with a content directly tunable as a function of the adopted growth temperature (100-400 °C). Concomitantly, nanosystems with hierarchical morphologies spanning from dendritic structures to quasi-1D sharp nanothorns, with controllable surface roughness and optical properties, could be effectively obtained. The fabricated materials were composed by pure β-MnO_2 at a deposition temperature of 100-300 °C, and by the co-presence of β-MnO_2 and Mn_2O_3 at 400 °C. The validity of the proposed preparation route is further highlighted by the fact that, at variance with the preparation of MnO_2 polymorphs involving templates, surfactants and reagents, it affords high purity products without any post-synthesis treatment, that could alter the desired structures [6].A thorough multi-technique approach enabled to investigate the interplay between the preparation conditions and the resulting system characteristics. Preliminary photo-induced hydrophilicity/photocatalytic functional tests, both in the solid and in the liquid phase, highlighted the possibility of finely tailoring MnO_2 nanomaterial performances, which resulted from a complex interplay between their nano-organization, F content and optical absorption. In addition, the use of Vis illumination instead of the UV one did not result in an appreciable performance decrease, paving the way to the use of natural sunlight to activate the target processes. The obtained results, which, to the best of our knowledge, have no precedents up to date on the target materials open challenging perspectives for the development of multi-functional photocatalysts for self-cleaning and antifogging applications, as well as for wastewater treatment.

Conflicts of interest

There are no conflicts to declare.

Acknowledgements

Padova University DOR 2016–2017, P-DiSC #03BIRD2016-UNIPD projects, HERALD Cost Action MP1402 - 37831 and ACTION post-doc fellowship are acknowledged for financial support. T.A. acknowledges a post-doctoral grant from the Research Foundation Flanders (FWO). Thanks are also due to Prof. Sara Bals (EMAT, University of Antwerp, Belgium), Prof. Romana Cerc Korošec and to Dr. Lev Matoh (University of Ljubljana, Slovenia), and to Prof. E. Bontempi (Brescia University, Italy). The work was also supported by EPSRC (award EP/R008841/1, EP/M024938/1).

Notes and references

1. K. Saravanakumar, V. Muthuraj and S. Vadivel, *RSC Adv.*, 2016, **6**, 61357-61366.
2. B. A. Pinaud, Z. B. Chen, D. N. Abram and T. F. Jaramillo, *J. Phys. Chem. C*, 2011, **115**, 11830-11838.
3. F. Li, P. Wangyang, A. Zada, M. Humayun, B. Wang and Y. Qu, *Mater. Res. Bull.*, 2016, **84**, 99-104.
4. S. R. Patil, B. H. Hameed, A. S. Škapin and U. L. Štangar, *Chem. Eng. J.*, 2011, **174**, 190-198.
5. S. Das, A. Samanta and S. Jana, *ACS Sustainable Chem. Eng.*, 2017, **5**, 9086-9094.
6. A. Baral, D. P. Das, M. Minakshi, M. K. Ghosh and D. K. Padhi, *ChemistrySelect*, 2016, **1**, 4277-4285.
7. D. Barreca, A. Gasparotto, C. Maccato, E. Tondello, U. L. Štangar and S. R. Patil, *Surf. Coat. Technol.*, 2009, **203**, 2041-2045.
8. D. Bekermann, A. Gasparotto, D. Barreca, C. Maccato, M. Rossi, R. Matassa, I. Cianchetta, S. Orlanducci, M. Kete and U. Lavrenčič Štangar, *Cryst. Growth Des.*, 2012, **12**, 5118-5124.
9. W. Tang, M. Yao, Y. Deng, X. Li, N. Han, X. Wu and Y. Chen, *Chem. Eng. J.*, 2016, **306**, 709-718.
10. F. Gao, X. Tang, H. Yi, C. Chu, N. Li, J. Li and S. Zhao, *Chem. Eng. J.*, 2017, **322**, 525-537.
11. S. A. Alzahrani, S. A. Al-Thabaiti, W. S. Al-Arjan, M. A. Malik and Z. Khan, *J. Mol. Struct.*, 2017, **1137**, 495-505.
12. J. Cao, Q. H. Mao, L. Shi and Y. T. Qian, *J. Mater. Chem.*, 2011, **21**, 16210-16215.
13. Y. L. Chan, S. Y. Pung, S. Sreekantan and F. Y. Yeoh, *J Exp Nanosci*, 2016, **11**, 603-618.
14. B. Tang, G. L. Wang, L. H. Zhuo and J. C. Ge, *Nanotechnol.*, 2006, **17**, 947-951.
15. R. E. John, A. Chandran, M. Thomas, J. Jose and K. C. George,

Appl. Surf. Sci., 2016, **367**, 43-51.
16. M. Sun, B. Lan, T. Lin, G. Cheng, F. Ye, L. Yu, X. L. Cheng and X. Y. Zheng, *CrystEngComm*, 2013, **15**, 7010-7018.
17. J. T. Sampanthar, J. Dou, G. G. Joo, E. Widjaja and L. Q. H. Eunice, *Nanotechnol.*, 2007, **18**, 025601.
18. G. Cheng, S. Xie, B. Lan, X. Zheng, F. Ye, M. Sun, X. Lu and L. Yu, *J. Mater. Chem. A*, 2016, **4**, 16462-16468.
19. D. M. Robinson, Y. B. Go, M. Mui, G. Gardner, Z. J. Zhang, D. Mastrogiovanni, E. Garfunkel, J. Li, M. Greenblatt and G. C. Dismukes, *J. Am. Chem. Soc.*, 2013, **135**, 3494-3501.
20. S. Balamurugan, A. Rajalakshmi and D. Balamurugan, *J. Alloys Compd.*, 2015, **650**, 863-870.
21. B. S. Singu and K. R. Yoon, *J. Alloys Compd.*, 2017, **695**, 771-778.
22. A. Kumar, A. Sanger, A. Kumar, Y. Kumar and R. Chandra, *Electrochim. Acta*, 2016, **220**, 712-720.
23. J. A. Dawson and I. Tanaka, *ACS Appl. Mater. Interfaces*, 2014, **6**, 17776-17784.
24. J. B. Jia, P. Y. Zhang and L. Chen, *Catal Sci Technol*, 2016, **6**, 5841-5847.
25. F. Mattelaer, T. Bosserez, J. Ronge, J. A. Martens, J. Dendooven and C. Detavernier, *RSC Adv.*, 2016, **6**, 98337-98343.
26. H.-W. Chang, Y.-R. Lu, J.-L. Chen, C.-L. Chen, J.-F. Lee, J.-M. Chen, Y.-C. Tsai, C.-M. Chang, P.-H. Yeh, W.-C. Chou, Y.-H. Liou and C.-L. Dong, *Nanoscale*, 2015, **7**, 1725-1735.
27. Z. Sun, S. Firdoz, E. Ying-Xuan Yap, L. Li and X. Lu, *Nanoscale*, 2013, **5**, 4379-4387.
28. J. Zhou, H. Zhao, X. Mu, J. Chen, P. Zhang, Y. Wang, Y. He, Z. Zhang, X. Pan and E. Xie, *Nanoscale*, 2015, **7**, 14697-14706.
29. G. A. M. Ali, M. M. Yusoff, E. R. Shaaban and K. F. Chong, *Ceram. Int.*, 2017, **43**, 8440-8448.
30. C. L. Yu, G. Li, L. F. Wei, Q. Z. Fan, Q. Shu and J. C. Yu, *Catal. Today*, 2014, **224**, 154-162.
31. Z. Geng, Y. Wang, J. Liu, G. Li, L. Li, K. Huang, L. Yuan and S. Feng, *ACS Appl. Mater. Interfaces*, 2016, **8**, 27825-27831.
32. S. Saha and A. Pal, *Sep Purif Technol*, 2014, **134**, 26-36.
33. X. P. Li, J. Liu, Y. H. Zhao, H. J. Zhang, F. P. Du, C. Lin, T. J. Zhao and Y. H. Sun, *ChemCatChem*, 2015, **7**, 1848-1856.
34. N. Kumar, A. Sen, K. Rajendran, R. Rameshbabu, J. Ragupathi, H. A. Therese and T. Maiyalagan, *RSC Adv.*, 2017, **7**, 25041-25053.
35. Y. Yin, R. Huang, W. Zhang, M. Zhang and C. Wang, *Chem. Eng. J.*, 2016, **289**, 99-105.
36. U. Černigoj, U. L. Štangar, P. Trebše, U. O. Krašovec and S. Gross, *Thin Solid Films*, 2006, **495**, 327-332.
37. L. Li, X. H. Feng, Y. Nie, S. G. Chen, F. Shi, K. Xiong, W. Ding, X. Q. Qi, J. S. Hu, Z. D. Wei, L. J. Wan and M. R. Xia, *ACS Catal.*, 2015, **5**, 4825-4832.
38. D. Y. Li, J. Yang, W. X. Tang, X. F. Wu, L. Q. Wei and Y. F. Chen, *RSC Adv.*, 2014, **4**, 26796-26803.
39. X.-M. Liu, S.-Y. Fu and C.-J. Huang, *Powder Technol.*, 2005, **154**, 120-124.
40. J. F. Wang, L. J. Deng, G. Zhu, L. P. Kang, Z. B. Lei and Z. H. Liu, *CrystEngComm*, 2013, **15**, 6682-6689.
41. A. R. Merritt, R. Rajagopalan and J. D. Carter, *Thin Solid Films*, 2014, **556**, 28-34.
42. L. Armelao, D. Barreca, G. Bottaro, A. Gasparotto, C. Maccato, E. Tondello, O. I. Lebedev, S. Turner, G. Van Tendeloo, C. Sada and U. Lavrenčič Štangar, *ChemPhysChem*, 2009, **10**, 3249-3259.
43. X. J. Xing, Y. P. Yu, L. M. Xu, S. X. Wu and S. W. Li, *J. Phys. Chem. C*, 2008, **112**, 15526-15531.
44. S. Islam, M. H. Alfaruqi, V. Mathew, J. Song, S. Kim, S. Kim, J. Jo, J. P. Baboo, D. T. Pham, D. Y. Putro, Y.-K. Sun and J. Kim, *J. Mater. Chem. A*, 2017, **5**, 23299-23309.
45. A. Gasparotto, D. Barreca, D. Bekermann, A. Devi, R. A. Fischer, C. Maccato and E. Tondello, *J. Nanosci. Nanotechnol.*, 2011, **11**, 8206-8213.
46. N. Haddad, Z. Ben Ayadi, H. Mahdhi and K. Djessas, *J. Mater. Sci. - Mater. Electron.*, 2017, **28**, 15457-15465.
47. S. Aydogu, M. B. Coban and G. Cabuk, *Appl. Phys. A*, 2017, **123**, 409.
48. G. Carraro, D. Barreca, D. Bekermann, T. Montini, A. Gasparotto, V. Gombac, C. Maccato and P. Fornasiero, *J. Nanosci. Nanotechnol.*, 2013, **13**, 4962-4968.
49. A. Gasparotto, D. Barreca, D. Bekermann, A. Devi, R. A. Fischer, P. Fornasiero, V. Gombac, O. I. Lebedev, C. Maccato, T. Montini, G. Van Tendeloo and E. Tondello, *J. Am. Chem. Soc.*, 2011, **133**, 19362-19365.
50. G. Carraro, A. Gasparotto, C. Maccato, E. Bontempi, O. I. Lebedev, C. Sada, S. Turner, G. Van Tendeloo and D. Barreca, *RSC Adv.*, 2014, **4**, 52140-52146.
51. R. Jin, H. Liu, Y. Guan, J. Zhou and G. Li, *CrystEngComm*, 2015, **17**, 7717-7722.
52. D. Barreca, G. Carraro, E. Fois, A. Gasparotto, F. Gri, R. Seraglia, M. Wilken, A. Venzo, A. Devi, G. Tabacchi and C. Maccato, *J. Phys. Chem. C*, 2018, **122**, 1367-1375.
53. D. Barreca, G. Carraro, A. Gasparotto, C. Maccato, C. Sada, A. P. Singh, S. Mathur, A. Mettenbörger, E. Bontempi and L. E. Depero, *Int. J. Hydrogen Energy*, 2013, **38**, 14189-14199.
54. P. Schlossmacher, D. O. Klenov, B. Freitag and H. S. von Harrach, *Micros. Today*, 2010, **18**, 14-20.
55. S. Jana, S. Pande, A. K. Sinha, S. Sarkar, M. Pradhan, M. Basu, S. Saha and T. Pal, *J. Phys. Chem. C*, 2009, **113**, 1386-1392.
56. L. Armelao, D. Barreca, G. Bottaro, A. Gasparotto, C. Maccato, C. Maragno, E. Tondello, U. L. Stangar, M. Bergant and D. Mahne, *Nanotechnol.*, 2007, **18**, 375709.
57. Pattern N° 024-0735, JCPDS (2000)
58. Pattern N° 041-1442, JCPDS (2000)
59. M. Liu, G. J. Zhang, Z. R. Shen, P. C. Sun, D. T. Ding and T. H. Chen, *Solid State Sci*, 2009, **11**, 118-128.
60. J. Xu, J. B. Liu, B. Huang, S. N. Li and B. X. Liu, *Acta Mater.*, 2017, **131**, 88-97.
61. M. J. Young, A. M. Holder, S. M. George and C. B. Musgrave, *Chem. Mater.*, 2015, **27**, 1172-1180.
62. J. A. Dawson, H. Chen and I. Tanaka, *ACS Appl Mater Interfaces*, 2015, **7**, 1726-1734.
63. Y. Meng, W. Song, H. Huang, Z. Ren, S. Y. Chen and S. L. Suib, *J. Am. Chem. Soc.*, 2014, **136**, 11452-11464.
64. S. Liu, J. Yu, B. Cheng and M. Jaroniec, *Adv. Colloid Interface Sci.*, 2012, **173**, 35-53.

Electronic Supplementary Information

for

Multi-functional MnO_2 nanomaterials for photo-activated applications by a plasma-assisted fabrication route

Davide Barreca,*[a] Filippo Gri,[b] Alberto Gasparotto,[b] Giorgio Carraro,[b] Lorenzo Bigiani,[b] Thomas Altantzis,[c] Bostjan Zener,[d] Urška Lavrenčič Štangar,[d,e] Bruno Alessi,[f] Dilli Babu Padmanaban,[f] Davide Mariotti[f] and Chiara Maccato*[b]

[a] *CNR-ICMATE and INSTM, Department of Chemical Sciences, Padova University, Via Marzolo 1, 35131 Padova, Italy*

[b] *Department of Chemical Sciences, Padova University and INSTM, Via Marzolo 1, 35131 Padova, Italy*

[c] *EMAT, University of Antwerp, 2020 Antwerp, Belgium*

[d] *Faculty of Chemistry and Chemical Technology, University of Ljubljana, 1000 Ljubljana, Slovenia*

[e] *Laboratory for Environmental and Life Sciences, University of Nova Gorica, 5000 Nova Gorica, Slovenia*

[f] *Nanotechnology & Integrated Bio-Engineering Centre (NIBEC), Ulster University, BT37 0QB, UK*

* Corresponding authors. E-mail: davide.barreca@unipd.it; chiara.maccato@unipd.it

§ S-1. Characterization

§ S-1.1 X-ray photoelectron spectroscopy (XPS)

The surface C1s signal (Fig. S1) could be fitted by means of four distinct components. Bands (I) and (II), centered at BE = 284.8 eV and 286.3 eV, respectively, were attributed to adventitious carbon contaminations and to surface C-O moieties.[1, 2] The two components located at 289.0 eV (III) and 292.6 eV (IV) were mainly ascribed to CF and CF_2 residuals from the used Mn precursor.[3] The surface C1s photopeak was reduced to noise level after 5 min Ar^+ erosion, indicating thus that carbon presence was limited to the sample surface and highlighting the purity of the obtained systems.

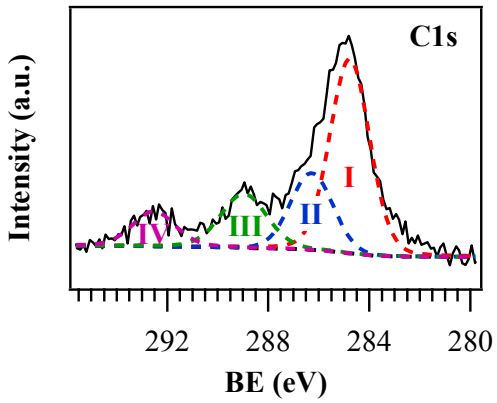

Figure S1. Surface C1s photopeak for a manganese oxide specimen grown at 200°C.

§ S-1.2 Energy dispersive X-ray spectroscopy (EDXS)

EDXS compositional analyses were carried out both in plane and in cross-sectional mode. Fig. S2a reports a representative spectrum, in which O, Mn and F signals could be clearly discerned. Na, Si and Sn signals originate from the growth substrate. Cross-sectional analyses (Fig. S2b) evidenced an almost parallel distribution of O, Mn and F throughout the deposit, suggesting their common chemical origin and demonstrating a uniform in-depth fluorine distribution.

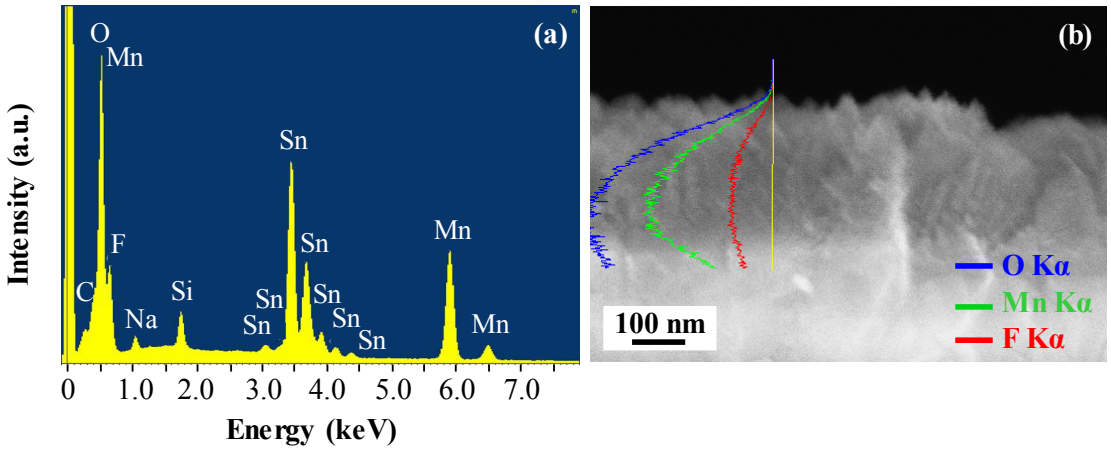

Figure S2. (a) EDXS spectrum for a manganese oxide sample deposited at 200°C. (b) Cross-sectional EDXS O Kα, Mn Kα and F Kα line-scans for the same specimen.

§ S-1.3 Atomic force microscopy (AFM)

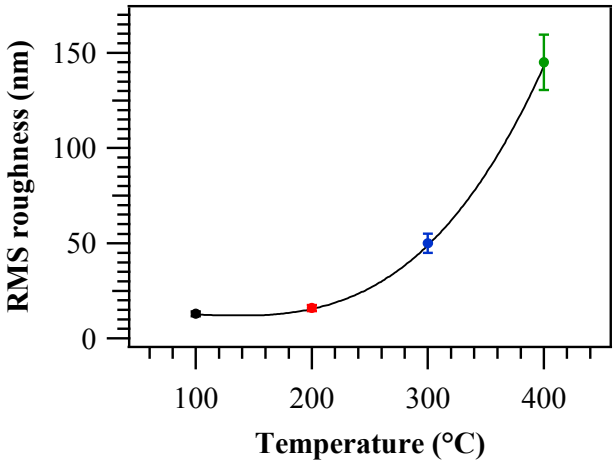

Figure S3. Evolution of the root mean square (RMS) roughness obtained by AFM measurements as a function of the adopted deposition temperature.

§ S-1.4 Kelvin probe (KP) and valence band XPS results

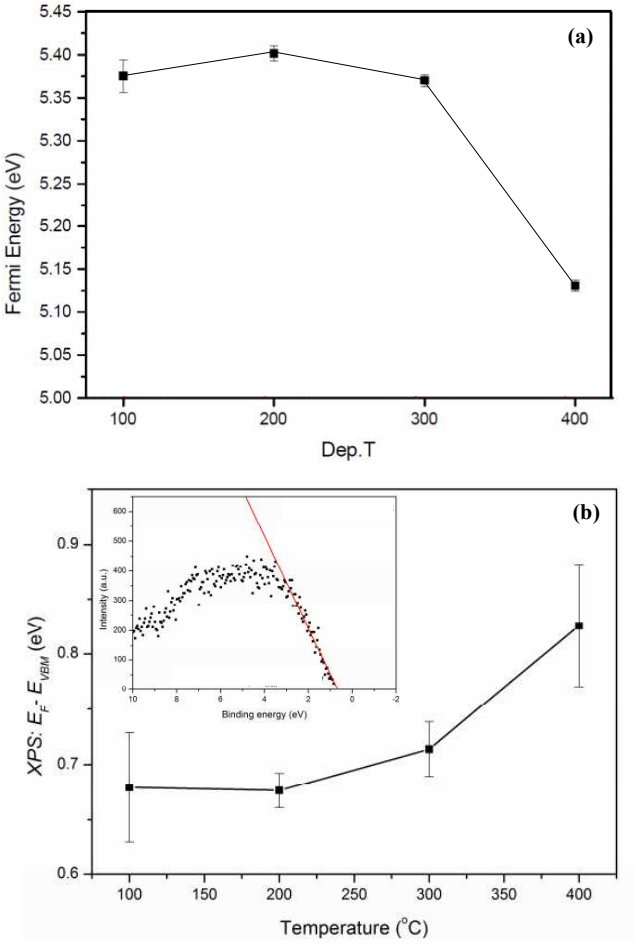

Figure S4. (a) Absolute Fermi energy obtained by KP. (b) Valence band onset with respect to the Fermi level as determined by XPS valence band measurements. In the inset, experimental data for the sample grown at 200° C are provided as an example.

§ S-1.5 Photocatalytic tests

The photocatalytic activity mechanism leading to the degradation of the target dye can be described as follows:[4-9]

$MnO_2 + h\nu \rightarrow MnO_2(e^-) + h^+$ (S1)

$h^+ + H_2O \rightarrow HO^\bullet$ (S2)

$e^- + O_2 \rightarrow O_2^{\bullet-}$ (S3)

$O_2^{\bullet-} + H_2O \rightarrow HO_2^\bullet + HO^\bullet$ (S4)

$O_2^{\bullet-} / HO^\bullet / HO_2^\bullet$ + organic pollutant $\rightarrow$ degradation products (S5)

Upon irradiation of the catalyst, holes (h^+) and electrons (e^-) are simultaneously generated in its valence and conduction bands, respectively (equation (S1)). Subsequently, holes reaction with water molecules results in the formation of hydroxyl radicals (equation (S2)). In turn, photogenerated electrons can be scavenged by dissolved O_2, yielding superoxide radical anions and generate $HO_2^\bullet$ and $HO^\bullet$ species (equations (S3) and (S4)). Finally, the target organic pollutant can be effectively oxidized by the photogenerated radicals, generating mineralized products (CO_2, H_2O,…) (equation (S5)) .

	k **(min^{-1})**	***t*$_{1/2}$ (min)**
UV irradiation	(0.025±0.001)	28
Vis irradiation	(0.022±0.002)	31

Table S1. Comparison of first-order reaction rate constants and half-life times for the photobleaching of Plasmocorinth B solutions under UV and Vis illumination for a β-MnO_2 specimen deposited at 200°C.

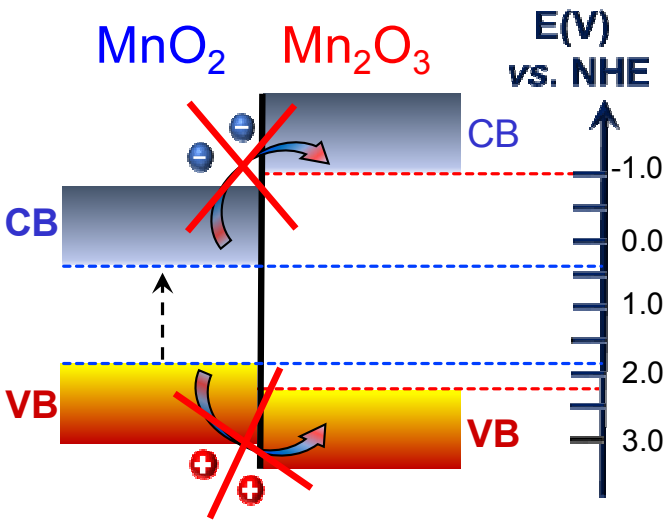

Figure S5. Schematic representation of the band structures of β-MnO_2 and cubic Mn_2O_3 [10, 11].

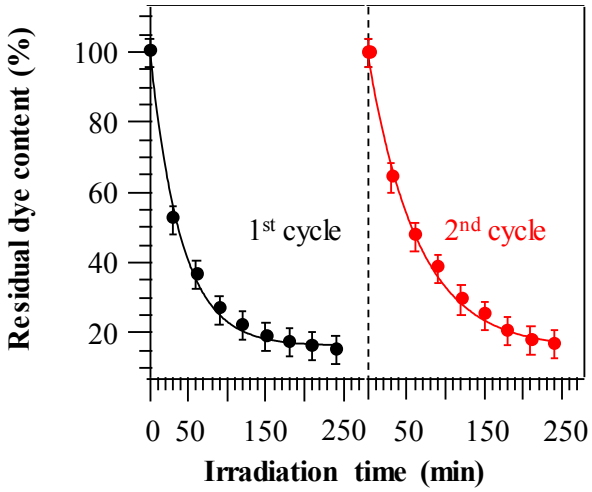

Figure S6. Different UV photodegradation cycles of Plasmocorinth B for a MnO_2 sample fabricated at a growth temperature of 200°C.

References

1. J. F. Moulder, W. F. Stickle, P. E. Sobol and K. D. Bomben, *Handbook of X-ray Photoelectron Spectroscopy*, Perkin Elmer Corporation, Eden Prairie, MN, USA, 1992.
2. D. Briggs and M. P. Seah, *Practical surface analysis: Auger and X-ray photoelectron spectroscopy*, John Wiley & Sons: New York, 2nd ed., 1990.
3. G. Carraro, A. Gasparotto, C. Maccato and D. Barreca, *Surf. Sci. Spectra*, 2013, **20**, 9-16.
4. K. Saravanakumar, V. Muthuraj and S. Vadivel, *RSC Adv.*, 2016, **6**, 61357-61366.
5. L. Armelao, D. Barreca, G. Bottaro, A. Gasparotto, C. Maccato, C. Maragno, E. Tondello, U. L. Stangar, M. Bergant and D. Mahne, *Nanotechnol.*, 2007, **18**, 375709.
6. N. Kumar, A. Sen, K. Rajendran, R. Rameshbabu, J. Ragupathi, H. A. Therese and T. Maiyalagan, *RSC Adv.*, 2017, **7**, 25041-25053.
7. A. Baral, D. P. Das, M. Minakshi, M. K. Ghosh and D. K. Padhi, *ChemistrySelect*, 2016, **1**, 4277-4285.
8. K. A. M. Ahmed, H. Peng, K. Wu and K. Huang, *Chem. Eng. J.*, 2011, **172**, 531-539.
9. S. Das, A. Samanta and S. Jana, *ACS Sustainable Chem. Eng.*, 2017, **5**, 9086-9094.
10. Y. L. Chan, S. Y. Pung, S. Sreekantan and F. Y. Yeoh, *J Exp Nanosci*, 2016, **11**, 603-618.
11. F. Li, P. Wangyang, A. Zada, M. Humayun, B. Wang and Y. Qu, *Mater. Res. Bull.*, 2016, **84**, 99-104.

Multi-functional MnO_2 nanomaterials for photo-activated applications by a plasma-assisted fabrication route

Davide Barreca,*[a] Filippo Gri,[b] Alberto Gasparotto,[b] Giorgio Carraro,[b] Lorenzo Bigiani,[b] Thomas Altantzis,[c] Bostjan Zener,[d] Urška Lavrenčič Štangar,[d,e] Bruno Alessi,[f] Dilli Babu Padmanaban,[f] Davide Mariotti[f] and Chiara Maccato*[b]

Statement to specify the contribution of each co-author

Davide Barreca planned the work and had a major role in writing the paper.

Filippo Gri carried out the plasma-assisted synthesis of the target MnO_2 nanomaterials.

Alberto Gasparotto performed optical absorption analyses and the pertaining data elaboration.

Giorgio Carraro and **Bostjan Zener** carried out photo-activated functional tests on the developed nanosystems.

Lorenzo Bigianiperformed XPS analyses on the target systems.

Thomas Altantzis performed and interpreted TEM and related measurements on MnO_2 nanosystems.

Urška Lavrenčič Štangar and **Davide Mariotti** supervised photocatalytic measurements and KP/XPS valence band measurements, respectively, and wrote the pertaining parts of the manuscript.

Bruno Alessi and **Dilli Babu Padmanaban** carried out KP/XPS valence band measurements and organized the pertaining experimental data.

Chiara Maccato performed and interpreted FE-SEM, EDXS and AFM measurements on prepared nanosystems and had a major role in finalizing the paper.

All the co-authors gave their personal contribution to the paper design and writing.